INT. J. NUM. METH. HEAT FLUID FLOW, VOL. 5, 647–663 (1995)

SIMULATION OF ICE COVER MELTING IN TURBULENT FLOW

RAAFAT G. SAADÉ AND SEMAAN SARRAF

Dept. of Civil Engineering, Concordia University, 1455 de Maisonneuve Blvd. West, Montreal, Quebec, Canada

ABSTRACT

In Northern Regions, ice covers that form on rivers, streams, and lakes with the onset of winter, cause various problems related to winter navigation and pollution dispersion among others. Warm water, from industrial plants, discharged into these rivers cause partial or total melting of the ice cover over considerable distances. The present work investigates the melting of a thin non-uniform ice cover subject to varying water and air temperatures under turbulent flow conditions. A two-dimensional depth averaged turbulence model coupled with a heat transfer model is used to simulate laboratory conditions of ice cover melting. Computational results were compared with experimental investigations. The average melting of the ice cover was found to be in close agreement with the experimental measurements with the exception of the leading edge region.

KEY WORDS Turbulence Ice cover Melting Dispersion MacCormack St Venant Two-dimensional Leading edge

NOMENCLATURE

C_1	empirical coefficient
C_2	empirical coefficient
C_c	coefficient for ice cover reduction in conductive heat transfer
C_e	coefficient for ice cover reduction in evapo-condensation heat flux
C_{wi}	heat transfer constant water to ice, in $W\,s^{-0.2}\,m^{-2.6}\,C^{-1}$
e_a	air vapour pressure, in mb
e_s	saturation vapour pressure, in mb
G	source term
h	water depth, in m
k	turbulent kinetic energy
K_i	ice thermal conductivity, in $W\,m^{-1}\,s^{-1}\,°C^{-1}$
n	combined Manning's coefficient
n_b	Manning's coefficient of river bed
n_i	Manning's coefficient of the underside of ice cover
R	hydraulic radius
S_{fx}	friction slope in the x-direction
S_{fy}	friction slope in the y-direction
t	time
T	water temperature, in °C
u	flow velocity component in x-direction, in $m\,s^{-1}$
V_a	wind velocity at 2 m above surface, in $m\,s^{-1}$
v	flow velocity component in y-direction, in $m\,s^{-1}$
x	spatial coordinate, longitudinal direction
y	spatial coordinate, transversal direction
Z_0	river or channel bed elevation
α	surface albedo
θ	ice cover thickness, in m
θ_{wi}	heat flux, water to ice cover, in $W\,m^{-2}\,s^{-1}$
ε	dissipation of turbulent kinetic energy
ε_s	emissivity of water or ice surface
Γ_T	turbulent heat diffusion coefficient
τ_l	bulk extinction coefficient, in cm^{-1}
τ_{bx}	bottom shear stress in the x-direction
τ_{by}	bottom shear stress in the y-direction
τ_{sx}	surface shear stress in the x-direction
τ_{sy}	surface shear stress in the y-direction
τ_{ij}	turbulent stresses, in vector notation
ϕ_b	effective back radiation
ϕ_{ba}	atmospheric radiation
ϕ_{bn}	net atmospheric radiation

0961–5539/95/070647–17$2.00

Received January 1993
Revised May 1994

ϕ_{bs} longwave radiation emitted by the river surface
ϕ_c conductive heat transfer
ϕ_e evapo-condensation flux
ϕ_{lat} latitude on earth's surface, in degrees
ϕ_{ri} incoming shortwave radiation
ϕ_s net shortwave radiation
ϕ_{sp} shortwave penetration into the waterbody
ν_t turbulent viscosity

INTRODUCTION

In Northern Regions, ice covers are formed on rivers, lakes and streams during the winter season. The yearly re-occurrence of this natural phenomenon causes a number of problems related to winter transportation, power generation, water supply, municipal and industrial wastewater disposal and flood control. Of major concern to hydraulic and environmental engineers is the development of methods to control the evolution of ice covers. Besides the traditional method of mechanically breaking the ice cover, engineers are continuously looking for alternatives which enable the extension of the navigation season all year round. The use of waste heat from industrial and municipal sources could be considered an alternative for suppressing the formation of an ice cover or for reducing its thickness, thereby facilitating ice management and extending winter navigation period.

Most of the research work done on freezing and melting of ice covers has been directed towards Arctic and Sub Arctic seas applications. Only a few investigations have been carried out on river ice cover melting. Methods to predict river ice formation have been developed based on analyses of meteorological and river flow records. Bilello[4] made an attempt to adapt such relationship to predict river and lake ice formation under specified meteorological and flow conditions. This semi-empirical method is based on a simplified heat transfer theory involving the temperature differences between the water surface and the air. Other methods to estimate the length of ice-free reaches in rivers and channels below thermal outfalls are at hand[8,14,19]. In these studies, it has been assumed that an ice cover can only exist where river temperature has reached the freezing point. Whereas, field observations have shown that, an ice cover can exist indeed with the ambient water temperature several tenths of a degree above 0°C depending on air temperatures, wind and other meteorological conditions[12]. Marsh and Prowse[10] presented a comparison of four different techniques for calculating heat transfer coefficients under an ice jam. The heat transfer coefficient calculated from the Colburn analogy method was shown to be in closest agreement to those using a temperature decay approach.

Few numerical models on ice cover melting were attempted. Shen and Chiang[21] developed a one-dimensional model of ice cover growth and decay on the St. Lawrence river using a uniform velocity field. A complete ice cover and open water heat transfer formulation was also included. Sarraf presented[20] a two-dimensional model for river ice cover melting due to a thermal effluent. Shen *et al.* developed[22] a one-dimensional numerical model, for simulating flow and ice conditions in a river such that the thermal growth and decay of an ice cover is calculated by a quasi-steady finite difference method.

Field measurements carried out by Ashton[2] at the Mississippi River as well as by Marsh and Prowse[10] at the Liard River have shown that the water temperature variation over the depth under an ice cover is negligible. In light of this, it can be safely assumed that the flow regime can be suitably described by the depth-averaged equations of motion.

In the present work, the flow and temperature fields are obtained by solving the two-dimensional depth averaged continuity, momentum, and heat energy equations. The present work focuses primarily on the effects of warm water on the two-dimensional melting of a non-uniform thin ice cover floating over turbulent flow conditions. A two-dimensional depth-averaged turbulence model is integrated with the hydrodynamic and temperature routines to estimate the turbulent flow characteristics.

GOVERNING EQUATIONS

Hydrodynamic conditions are simulated using the St. Venant shallow water equations. These are obtained by integrating the Navier–Stokes equations over the water depth using the hydrostatic assumption and taking into account the presence of an ice cover. The depth-averaged continuity, momentum, turbulence energy and its rate of dissipation, and temperature equations in conservative form are expressed in vector form as follows[18]:

$$\frac{\partial \psi_t}{\partial t} + \frac{\partial \psi_x}{\partial x} + \frac{\partial \psi_y}{\partial y} = F \tag{1}$$

where

$$\psi_t = \begin{bmatrix} h \\ uh \\ vh \\ kh \\ \varepsilon h \\ Th \end{bmatrix}; \quad \psi_x = \begin{bmatrix} uh \\ u^2h - \dfrac{\tau_{xx}}{\rho} + PZ_T \\ uvh - \dfrac{\tau_{xy}}{\rho} \\ ukh - \dfrac{\nu_t h}{\sigma_k}\dfrac{\partial k}{\partial x} \\ u\varepsilon h - \dfrac{\nu_h h}{\sigma_\varepsilon}\dfrac{\partial \varepsilon}{\partial x} \\ uTh - \Gamma_T h \dfrac{\partial T}{\partial x} \end{bmatrix};$$

$$\psi_y = \begin{bmatrix} vh \\ uvh - \dfrac{\tau_{yx}}{\rho} \\ v^2h + PZ_T - \dfrac{\tau_{yy}}{\rho} \\ vkh - \dfrac{\nu_t h}{\sigma_k}\dfrac{\partial k}{\partial y} \\ v\varepsilon h - \dfrac{\nu_t h}{\sigma_\varepsilon}\dfrac{\partial \varepsilon}{\partial y} \\ vTh - \Gamma_T h \dfrac{\partial T}{\partial y} \end{bmatrix}; \quad F = \begin{bmatrix} 0 \\ \dfrac{\tau_{sx}}{\rho} - \dfrac{\tau_{bx}}{\rho} \\ \dfrac{\tau_{sy}}{\rho} - \dfrac{\tau_{by}}{\rho} \\ G + P_{kv} - \varepsilon h \\ C_1 \dfrac{\varepsilon}{k} G + P_{\varepsilon v} - C_2 \dfrac{\varepsilon^2 h}{k} \\ \phi \end{bmatrix} \tag{2}$$

in which h = water depth; T = water temperature; u = velocity in the x-direction; v = velocity in the y-direction; k = turbulent kinetic energy; ε = dissipation of k; ν_t = turbulent viscosity; G, P_{kv}, $P_{\varepsilon v}$, and ϕ = source terms; σ_ε, σ_k, C_1, and C_2 = empirical coefficients; $Z_T = [h + Z_0 + 0.92(\theta)]$, with Z_0 = river or channel bed elevation and θ = ice cover thickness; $P = gh/2$; Γ_T is the turbulent heat diffusion coefficient; and τ_{sx}, τ_{sy} and τ_{bx}, τ_{by} = surface and bottom shear stresses in x and y directions, respectively. Bottom shear stresses are given by:

$$\frac{\tau_{bx}}{\rho} = ghS_{fx} \tag{3}$$

$$\frac{\tau_{by}}{\rho} = ghS_{fy} \tag{4}$$

S_{fx} and S_{fy} are the friction slopes given by:

$$S_{fx} = \frac{n^2 uq}{R^{4/3}} \tag{5}$$

$$S_{fy} = \frac{n^2 vq}{R^{4/3}} \tag{6}$$

where

$$q = (u^2 + v^2)^{1/2} \tag{7}$$

R = hydraulic radius ($R = h$ for open water flow and $R = h/2$ for ice-covered flow). For open water flow, Manning coefficient is determined by the bed friction, while for ice covered flow a combined coefficient is required taking into account the roughness of the river bed as well as ice cover underside expressed as follows:

$$n = \left(\frac{n_b^{3/2} + n_i^{3/2}}{2}\right)^{2/3} \tag{8}$$

where n_b = bed roughness coefficient and n_i = ice bottom roughness coefficient.

To account for the effect of a floating ice cover, the hydrostatic pressure terms in the momentum equations were modified. The additional pressure due to the weight of the ice cover is considered by adding 92% of the ice thickness to the water depth. This value represents the density ratio between ice and water.

The turbulent diffusion heat flux coefficient Γ_T present in the heat equation is determined over the flow domain by:

$$\Gamma_T = \frac{\nu_t}{\sigma_T} \tag{9}$$

where ν_t = the turbulent viscosity; and σ_t = empirical constant equal to 0.5[11].

The depth averaged k–ε turbulence model, based on the Boussinesq eddy viscosity concept, has been adopted after McGuirk and Rodi[11]. This model characterizes the local state of turbulence by its turbulent kinetic energy k and its rate of dissipation ε. k and ε are computed using their corresponding transport equations (see (2)). The source terms found in the k and ε equations are evaluated as follows:

$$G = \frac{\nu_t}{h}\left[2\left(\frac{\partial uh}{\partial x}\right)^2 + 2\left(\frac{\partial vh}{\partial y}\right)^2 + \left(\frac{\partial uh}{\partial y} + \frac{\partial vh}{\partial x}\right)^2\right] \tag{10}$$

The term G represents the production of turbulent kinetic energy in the horizontal direction due to interactions of turbulent stresses with horizontal mean velocity gradients; and the empirical constants $\sigma_k = 1.0$, $\sigma_\varepsilon = 1.3$; $C_1 = 1.43$, and $C_2 = 1.92$. The values of these empirical constants are based on extensive examination of free turbulent flows and they can be used for flows near solid surfaces. A sensitivity study has shown that the calculations are most sensitive to the values of C_1 and C_2[17]. In addition to the turbulent production G, bottom roughness contributes significantly to the vertical velocity gradients which, by interaction with large turbulent shear stresses, produces turbulence energy in the vertical direction. This vertical turbulence energy production is absorbed in the P_{kv} and $P_{\varepsilon v}$ terms which are expressed as follows:

$$P_{kv} = \frac{C_f}{h} q^3 \tag{11}$$

$$P_{ev} = \frac{3.6C_2C_\mu^{1/2}C_f^{5/4}q^4}{h^2} \tag{12}$$

where C_f = empirical friction factor equal to 0.003.

The shear stress terms in the momentum equations are evaluated using the eddy viscosity concept. The latter is based on the assumption that the turbulent stresses are proportional to the mean velocity gradient. The depth-averaged turbulent stresses can then be calculated using the eddy viscosity concept, by the following expressions:

$$\frac{\tau_{xx}}{\rho} = \nu_t\left(2\frac{\partial uh}{\partial x}\right) - \frac{2}{3}kh \tag{13}$$

$$\frac{\tau_{xy}}{\rho} = \frac{\tau_{yx}}{\rho} = \nu_t\left(\frac{\partial uh}{\partial y} + \frac{\partial vh}{\partial x}\right) \tag{14}$$

$$\frac{\tau_{yy}}{\rho} = \nu_t\left(2\frac{\partial vh}{\partial y}\right) - \frac{2}{3}kh \tag{15}$$

where the turbulent viscosity ν_t is a function of the state of turbulence in the flow domain. The turbulent eddy viscosity is given in terms of the kinetic energy k, and its rate of dissipation ε, as follows:

$$\nu_t = C_\mu\frac{k^2}{\varepsilon} \tag{16}$$

where C_μ is an empirical constant equal to 0.09.

MELTING OF A SOLID ICE COVER

The growth and decay of an ice cover are a function of the heat budget components, mainly the heat transfer across the water–air, ice–air, and water–ice interfaces. The flux at the ice–air interface includes shortwave (solar) radiation, longwave radiation evapo-condensation flux and convective heat transfer. The meteorological factors that are used to determine these solar radiation components are cloud cover, air temperature, wind velocity and air vapour pressure. In the present study, heat transfer from precipitation or through the river bed is not considered as significant since its effect is assumed to be small in modelling the melting of ice cover by warm water. The evaluation of the heat flux components shown in *Figure 1* allows for the calculation of the change in ice cover thickness. These heat flux components are expressed as follows.

Shortwave solar radiation

The value of the net shortwave solar radiation that reaches the terrestrial surface, ϕ_s, is computed by[21]:

$$\phi_s = (\phi_{ri} - \phi_{rs}) = (1 - \alpha)\phi_{ri} \tag{17}$$

where $\alpha = 0.1$ is the value of the albedo expressing the portion of reflected or absorbed radiation by the water surface and which depends on the material behaviour of the ice cover; and ϕ_{ri} is the incident shortwave radiation. Studies at Lake Hefner, Oklahoma[1] showed that the water surface albedo ranged from 0.05 to 0.3 and was a strong function of solar altitude and depended to some extent on cloud conditions.

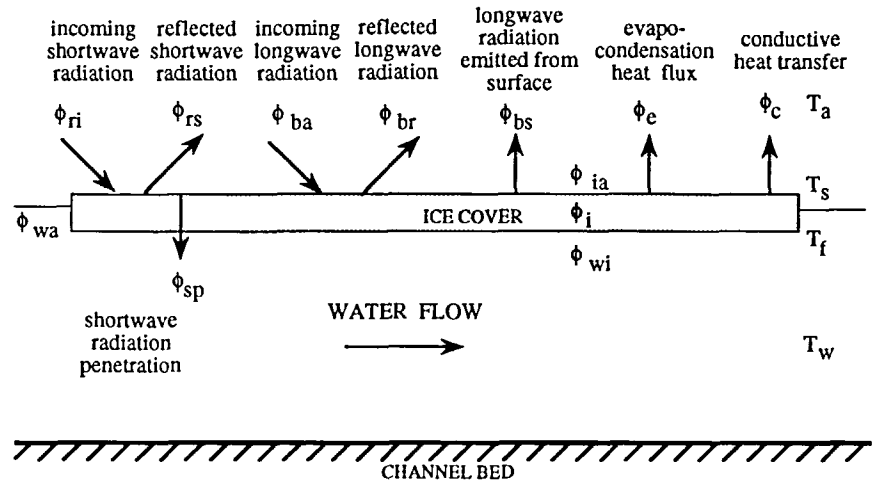

Figure 1 Heat budget at the channel surface

A portion of the shortwave radiation penetrates through the ice cover up to the river water surface. This penetration of shortwave radiation ϕ_{sp} is evaluated by:

$$\phi_{sp} = \beta_i \phi_s e^{-\tau i \theta} \tag{18}$$

where $\beta_i = 1.0$ is the fraction of the shortwave radiation which penetrates across the ice–water interface; and $\tau_i = 0.007$ is the bulk extinction coefficient, m^{-1}. This penetration of shortwave radiation across the water–ice interface can be considered an internal heat source to the water body.

Longwave radiation

The energy emitted by the water surface is principally in the form of longwave radiation. This longwave radiation depends on the surface temperature and it is determined by the Stephan–Boltzman relationship given by:

$$\phi_{bs} = \varepsilon_w \alpha T_w^4 \tag{19}$$

where T_w is the water temperature, K; and ε_w is the emissivity of the surface, 0.97. The value of ε_w was obtained from studies that were carried out at Lake Hefner. These studies have also established that the emissivity of water is independent of the temperature and concentration of dissolved solids[1].

The value of the net longwave radiation that reaches the terrestrial surface, ϕ_{ba}, is computed from an empirical equation which relates it with the atmospheric conditions[1]. Under clear sky conditions the longwave radiation ϕ_{ba} is expressed as follows:

$$\phi_{ba} = (c + d(e_a)^{1/2})\sigma T_a^4 \tag{20}$$

where T_a is the temperature of the air, K; σ is the Boltzman constant, $4.903 \times 1 \cdot^{-7}$ J cm^{-2} day^{-1}; e_a is the vapour pressure of the air, mb; c and d are empirical constants equal to 0.55 and 0.052, respectively. Under cloudy conditions the longwave radiation takes into account the cloudiness in the equation as follows:

$$\phi_{ba} = (1 + k_c C^2)(C + d(e_a)^{1/2})\sigma T_a^4 \tag{21}$$

where k_c is an empirical constant, 0.0017 and C is the cloudiness expressed in tenths.

Convective heat flux

Heat losses by convection are obtained from the difference of temperature across the water–ice and ice–air interfaces. The heat transfer across the ice–air interface will be a fraction C_c of that under free surface conditions. Experience and analyses of studies performed on convective heat transfer allow to state a simplified formula which takes into account the difference of temperature between the air and the water. The following expression proposed by Shen and Chiang[21] is used in this study:

$$\phi_c = C_c(K_n + 3.67V_a)(T_w - T_a) \tag{22}$$

where V_a is the wind speed at 2.0 m above ground level, m/s; C_c is the extinction coefficient equal to 1 for free surface conditions and equal to 0.5 for ice covered conditions; T_w is the water temperature in °C; T_a is the air temperature in °C; and K_n is a dimensionless constant which represents the portion of heat transfer due to free convection and depends on the air and water temperature defined as follows:

$$K_n = 8.0 + 0.35(T_w - T_a) \tag{23}$$

Evapo-condensation heat flux

The flux ϕ_e due to evapo-condensation is given by the following formula proposed by Shen & Chiang[21]:

$$\phi_e = C_e(1.56K_n + 6.08V_a)(e_s - e_a) \tag{24}$$

where e_s is the saturated vapour pressure, mb; C_e is the extinction coefficient for evapo-condensation; and e_a is the vapour pressure of the air, mb. Under the presence of an ice cover, the evaporation heat flux is taken as half due to the reduction in the evaporation process.

Melting at the top surface

Melting of the ice cover from the top surface is dependent on the meteorological conditions, mainly the air temperature, wind velocity, shortwave radiation, longwave radiation, evapo-condensation heat flux, and conductive heat transfer. The melting from the top surface of the ice cover is based on the heat transfer process occurring at the ice–air interface, and can be obtained from the following expression, given that the computed surface temperature of the ice cover $T_s \geqslant 0$°C:

$$\Sigma\phi_i = -\rho_i L_i \frac{d\theta}{dt} \tag{25}$$

where $\Sigma\phi_i$ = net heat flux at the ice–air interface which includes the net solar radiation (ϕ_s), the longwave radiation (ϕ_b), the evapo-condensation heat flux (ϕ_e), and the conductive heat transfer (ϕ_c); ρ_i = the density of ice, 920 Kg m^{-3} and L_i = latent heat of fusion of ice, 8×10^4 cal Kg^{-1}.

Melting at the bottom surface

Melting at the bottom surface of the ice cover occurs due to the heat transfer from the water body to the ice cover. The turbulent heat transfer from the water to the ice cover depends on the heat transfer coefficient at the underside of the ice cover, and the water temperature. The heat exchange processes, in addition to the meteorological conditions, play an important role in determining the amount of heat the water body absorbs or emits and the amount of ice that forms or melts at the bottom of the ice cover. The melting and thickening at the bottom surface

of the ice cover is governed by the energy balance at this surface expressed as follows:

$$K_i \frac{T_f - T_s}{\theta} - C_{wi} \frac{U^{0.8}}{D^{0.2}} (T_w - T_f) = \rho_i L_i \frac{\Delta\theta}{\Delta t} \tag{26}$$

where T_s = ice cover top surface temperature computed as function of the heat exchange with the atmosphere, °C; T_f = freezing point temperature, °C; T_w is the water temperature, °C; U is the average water velocity, m s^{-1}; $\Delta\theta/\Delta t$ is the rate of change of the thickness of the ice; D is the flow depth, m; and C_{wi} = 1622 W S$^{0.8}$ m$^{2.6}$ °C^{-1} = heat transfer coefficient at the water–ice interface, such that the second term in the equation represents the heat flux at the water–ice interface (ϕ_{wi}).

NUMERICAL FORMULATION

MacCormack scheme

The solution of the depth-averaged St. Venant equations is obtained by applying an explicit finite difference method based on the modified MacCormack time splitting scheme[3]. The scheme is forward time and central space differencing and involves the splitting of the two-dimensional operators into a sequence of two one-dimensional operators. Each operator is further split into a predictor–corrector sequence as follows:

$$L(\Delta t) = L_x(\Delta t_x) L_y(\Delta t_y) L'_y(\Delta t_y) L'_x(\Delta t_x) \tag{27}$$

where L_x and L_y are the one-dimensional backward finite-difference operators, L'_x and L'_y are the one-dimensional forward finite-difference operators and $\Delta t_x = \Delta t_y = \Delta t/2$ is the time interval. The L_x and L_y operators calculate the derivatives in the x and y directions respectively. Both the x and y derivatives are then split into two half-time steps. Each operator, L_x and L_y, consist of a predictor which discretizes the space derivatives using the backward differences and a corrector which discretizes the space derivatives using the forward differences. In the L_x operator, the solution is advanced by a time step Δt_x, as if the derivatives in the y-direction were absent, and then in the L_y operator by a time step Δt_y, omitting the derivatives in the x-direction. Also, in both operators, backward differences are used for the predictor and forward differences for the corrector. The discretized forms of the continuity and momentum equations using the MacCormack scheme are as follows.

Discretization of the L_x operator

Predictor sequence: backward difference

$$H^P_{ij} = H^0_{ij} - \frac{\Delta t_x}{\Delta x} (u^0_{ij} h^0_{ij} - u^0_{i-1,j} h^0_{i-1,j})$$

$$u^P_{ij} h^P_{ij} = u^0_{i,j} h^0_{i,j} - \frac{\Delta t_x}{\Delta x} (u^{0^{2h^0}}_{i,j\ i,j} - y^{0^2}_{i-1,j\ i-1,j}{}^{h^0}) + \frac{\Delta t_x}{\Delta x} \left[\left(\frac{\tau_{xx}}{\rho} \right)^0_{i,j} - \left(\frac{\tau_{xx}}{\rho} \right)^0_{i-1,j} \right]$$
$$+ gh \frac{\Delta t_x}{\Delta x} [(h + 0.92\theta)^0_{i,j} - (h + 0.92\theta)^0_{i-1,j}] + \Delta t_x \left[\left(\frac{\tau_{sx}}{\rho} \right)^0_{i,j} - \left(\frac{\tau_{bx}}{\rho} \right)^0_{i,j} \right] \tag{29}$$

$$v^P_{ij} h^P_{ij} = v^0_{i,j} h^0_{i,j} - \frac{\Delta t_x}{\Delta x} (u^0_{i,j} v^0_{i,j} h^0_{i,j} - u^0_{i-1,j} v^0_{i-1,j} h^0_{i-1,j}) + \frac{\Delta t_x}{\Delta x} \left[\left(\frac{\tau_{yx}}{\rho} \right)^0_{i,j} - \left(\frac{\tau_{yx}}{\rho} \right)^0_{i-1,j} \right] \tag{30}$$

Corrector sequence forward differences

$$H^C_{i,j} = H^P_{ij} - \frac{\Delta t_x}{\Delta x}\left(u^P_{i+1,j}h^P_{i+1,j} - u^P_{ij}h^P_{ij}\right) \tag{31}$$

$$u^C_{i,j}h^C_{i,j} = u^P_{ij}h^P_{ij} - \frac{\Delta t_x}{\Delta x}\left(u^{P2}_{i+1,j}h^P_{i+1,j} - u^{P2}_{i,j}h^P_{ij}\right) + \frac{\Delta t_x}{\Delta x}\left[\left(\frac{\tau_{xx}}{\rho}\right)^P_{i+1,j} - \left(\frac{\tau_{xx}}{\rho}\right)^P_{i,j}\right]$$
$$+ gh\frac{\Delta t_x}{\Delta x}\left[(h+0.92\theta)^P_{i+1,j} - (h+0.92\theta)^P_{i,j}\right] + \Delta t_x\left[\left(\frac{\tau_{sx}}{\rho}\right)^P_{i,j} - \left(\frac{\tau_{bx}}{\rho}\right)^P_{i,j}\right] \tag{32}$$

$$v^C_{i,j}h^C_{i,j} = v^P_{ij}h^P_{ij} - \frac{\Delta t_x}{\Delta x}\left(u^P_{i+1,j}v^P_{i+1,j}h^P_{i+1,j} - u^P_{ij}v^P_{i+1,j}h^P_{ij}\right) + \frac{\Delta t_x}{\Delta x}\left[\left(\frac{\tau_{yx}}{\rho}\right)^P_{i+1,j} - \left(\frac{\tau_{yx}}{\rho}\right)^P_{i,j}\right] \tag{33}$$

and

$$H^{n+1}_{i,j} = \tfrac{1}{2}(H^0_{i,j} + H^C_{i,j}); \qquad u^{n+1}_{i,j} = \tfrac{1}{2}(u^0_{i,j} + u^C_{i,j}); \qquad v^{n+1}_{i,j} = \tfrac{1}{2}(v^0_{i,j} + v^C_{i,j}) \tag{34}$$

Discretization of L_y *operator*

Predictor sequence: backward difference

$$H^P_{i,j} = H^0_{i,j} - \frac{\Delta t_y}{\Delta y}\left(v^0_{i,j}h^0_{i,j} - v^0_{i,j-1}h^0_{i,j-1}\right) \tag{35}$$

$$v^P_{i,j}h^P_{i,j} = v^0_{i,j}h^0_{i,j} - \frac{\Delta t_y}{\Delta y}\left(v^{02}_{i,j}h^0_{i,j} - v^{02}_{i,j-1}h^0_{i,j-1}\right) + \frac{\Delta t_y}{\Delta y}\left[\left(\frac{\tau_{yy}}{\rho}\right)^0_{i,j} - \left(\frac{\tau_{yy}}{\rho}\right)^0_{i,j-1}\right]$$
$$+ gh\frac{\Delta t_y}{\Delta y}\left[(h+0.92\theta)^0_{i,j} - (h+0.92\theta)^0_{i,j-1}\right] + \Delta t_y\left[\left(\frac{\tau_{sy}}{\rho}\right)^0_{i,j} - \left(\frac{\tau_{by}}{\rho}\right)^0_{i,j}\right] \tag{36}$$

$$u^P_{i,j}h^P_{i,j} = u^0_{i,j}h^0_{i,j} - \frac{\Delta t_y}{\rho}\left(u^0_{i,j}v^0_{i,j}h^0_{i,j} - u^0_{i,j-1}v^0_{i,j-1}h^0_{i,j-1}\right) + \frac{\Delta t_y}{\Delta y}\left[\left(\frac{\tau_{xy}}{\rho}\right)^0_{i,j} - \left(\frac{\tau_{xy}}{\rho}\right)^0_{i,j-1}\right] \tag{37}$$

Corrector sequence forward differences

$$H^C_{i,j} = H^P_{i,j} - \frac{\Delta t_y}{\Delta y}\left(v^P_{i,j+1}h^P_{i,j+1} - v^P_{i,j}h^P_{i,j}\right) \tag{38}$$

$$v^C_{i,j}h^C_{i,j} = v^P_{i,j}h^P_{i,j} - \frac{\Delta t_y}{\Delta y}\left(v^{P2}_{i,j+1}h^P_{i,j+1} - v^{P2}_{i,j}h^P_{i,j}\right) + \frac{\Delta t_y}{\Delta y}\left[\left(\frac{\tau_{yy}}{\rho}\right)^P_{i,j+1} - \left(\frac{\tau_{yy}}{\rho}\right)^P_{i,j}\right]$$
$$+ gh\frac{\Delta t_y}{\Delta y}\left[(h+0.92\theta)^P_{i,j+1} - (h+0.92\theta)^P_{i,j}\right] + \Delta t_y\left[\left(\frac{\tau_{sy}}{\rho}\right)^P_{i,j} - \left(\frac{\tau_{by}}{\rho}\right)^P_{i,j}\right] \tag{39}$$

$$u^C_{i,j}h^C_{i,j} = u^P_{i,j}h^P_{i,j} - \frac{\Delta t_y}{\Delta y}\left(u^P_{i,j+1}v^P_{i,j+1}h^P_{i,j+1} - u^P_{i,j}v^P_{i+1,j}h^P_{i,j}\right) + \frac{\Delta t_y}{\Delta y}\left[\left(\frac{\tau_{xy}}{\rho}\right)^P_{i,j+1} - \left(\frac{\tau_{xy}}{\rho}\right)^P_{i,j}\right] \tag{40}$$

and

$$H^{n+1}_{i,j} = \tfrac{1}{2}(H^0_{i,j} + H^C_{i,j}); \qquad u^{n+1}_{i,j} = \tfrac{1}{2}(u^0_{i,j} + u^C_{i,j}); \qquad v^{n+1}_{i,j} = \tfrac{1}{2}(v^0_{i,j} + v^C_{i,j}) \tag{41}$$

The stability conditions are determined by the Courant–Friedrichs–Lewy criterion which states that the maximum time step that can be used in the standard MacCormack scheme is the

minimum value of the following two terms:

$$\Delta t = \min\left[\frac{\Delta x}{u + \sqrt{gh}}, \frac{\Delta y}{u + \sqrt{gh}}\right] \tag{42}$$

Upwind scheme

The use of an upwind scheme is required when convection is dominant in the development of the temperature field and either the flow is closely aligned with the grid lines or no strong cross flow gradients are present[16]. The upwind scheme used is an explicit forward time difference method which takes into account the direction of the convecting velocity. The upwind scheme assumes the same value of the property of the grid point on the upwind side for the face of the computation cell[15].

BOUNDARY CONDITIONS

Boundary conditions at the inlets, outlets and solid surfaces need to be specified. The velocity and temperature are specified at the inlets to the river, while the water depth is specified at the outlet of the river. At solid surfaces, the velocity in both directions u and v, the water depth h, the temperature T, the turbulent kinetic energy k and the rate of its dissipation ε, and the turbulent viscosity v_t should be imposed. The normal gradients of u, v and k at solid surfaces are set to zero. The temperature gradients are also zero since negligible heat transfer through the wall is assumed in most hydraulic problems. The walls are assumed to be adiabatic walls, where the heat and concentration flux are taken as zero. Also, the normal gradients of the water depth, ice cover thickness, and hydraulic radius are set to zero at all the cell adjacent to the wall.

Boundary conditions for k and ε require special treatment at solid surfaces[6]. In the near-wall region, the boundary layer thickness is small relative to the size of the discretized domain. Therefore, flow information at the cell nearest to the wall should be approximated using the law of the wall. To derive expressions for k and ε for the cell nearest to a solid surface, it is assumed that convection and diffusion are negligible and the turbulence energy production and the kinetic energy dissipation rate are in local equilibrium, and the turbulent shear stress is nearly constant and equal to the wall shear stress. Under these conditions and by applying the law of the wall, ε in the near-wall region and the shear stress τ_w at the solid surface can be determined as follows:

$$\varepsilon_w = \frac{U_*^3}{\kappa y_w} \tag{43}$$

$$\left\langle \frac{\tau}{\rho} \right\rangle_w = \frac{U_* \kappa u_w}{\ln(y_0/z_0)^2} \tag{44}$$

where k_w, ε_w = turbulent kinetic energy and rate of dissipation, respectively, in the near-wall region; u_w = resultant velocity parallel to the wall; U_* = resultant friction velocity; κ = Von Karman constant; $y_0 = \Delta y/2$ = half the grid spacing; z_0 = channel roughness height; and y_w = distance from the wall to the centre of the nearest cell (half the grid spacing).

The velocity u_w and the turbulent kinetic energy k_w, in the wall region, are calculated from their corresponding transport expressions as given by (2). However, ε in the k equation is evaluated by the following expression to account for the large increase in the dissipation rate that occurs in the near wall region[6]:

$$\varepsilon = \frac{U_*^3}{k y_w} \ln\left(\frac{y_0}{Z_0}\right) \tag{45}$$

MODEL APPLICATIONS AND RESULTS

The numerical model described herein is used to simulate laboratory experiments where a thin non-uniform ice cover was allowed to melt. However, first the hydrothermal computations were verified against experimental measurements and other modelling work calculations. Computed and measured ice cover melting characteristics were later compared.

Hydrodynamic and hydrothermal verification

Accurate hydrodynamic and dispersion computations are essential for the simulation of ice cover melting. These computations were verified by simulating an effluent discharge at right angles to the channel flow. The water depth is imposed at 5.0 m. The main channel width is taken as 50 m while that of the side discharge 5 m. The flow domain is fitted into a rectangular uniform grid of 120 by 20 cells of 2.5 m by 2.5 m dimensions.

The computed velocity distribution at steady state conditions and for velocity ratio $R = 2$ is illustrated in *Figure 2*. This Figure shows the influence of the side discharge on the main channel flow. Three affected regions are identified: upstream of the side discharge; the near field region extending 100 m downstream of the side discharge; and the far field region. Due to the side discharge blockage effect on the main channel flow, the water level rises in the upstream region. However, the relative increase in the velocity at the proximity of the side discharge, and the fact that the side discharge is perpendicular to the main channel flow, a recirculation region develops immediately downstream of the side discharge such that the water level drop in that region. Towards the far field region, the velocity distribution gradually becomes uniform accompanied with a gradual increase in the water level.

Figure 3 shows the computed and measured isotherms for a velocity ratio $R = 2$. These isotherms are of particular interest to environmentalists and ice engineers since they show the zones and extent of thermal pollution and consequently ice cover melting. The general behaviour of the computed isotherms correspond well with the measured ones. The penetration of temperature into the main channel and the region that this increase in temperature covers is certainly predicted correctly in the streamwise and lateral directions.

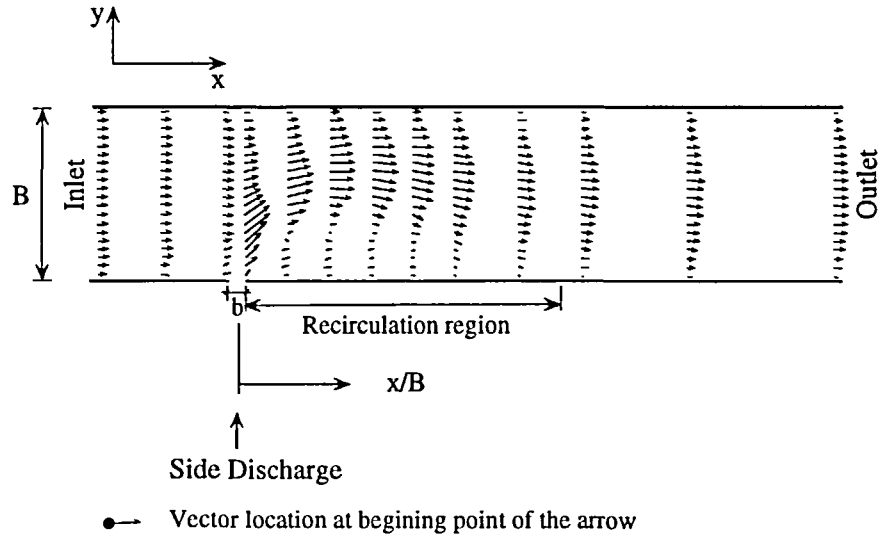

Figure 2 Computed velocity distribution for velocity ratio $R = 2$

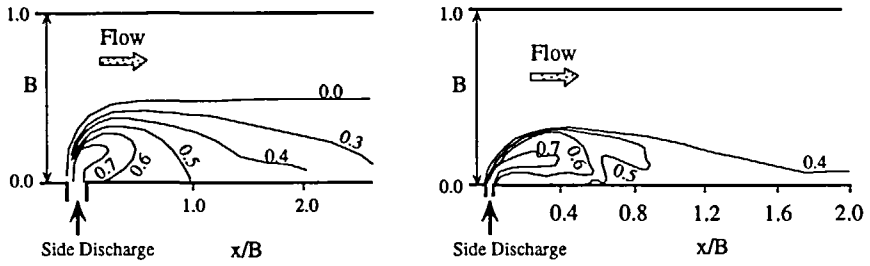

Figure 3 Computed and measured isotherms for velocity ratio $R = 2$

Table 1 Comparison of hydrodynamic computations (jet trajectory penetration to side discharge width ratio)

Velocity ratio	Carter[5]	McGuirk *et al.*[11]	Model
2	5.0	3.0	6.1
5	16.5	11.0	18.5
10	40.0	35.0	27.0

Table 2 Comparisons of hydrothermal computations (dilution)

Velocity ratio	Carter[5]	McGuirk *et al.*[11]	Model
2	40.0	40.0	40.0
5	41.0	34.0	50.0
10	45.0	36.0	60.0

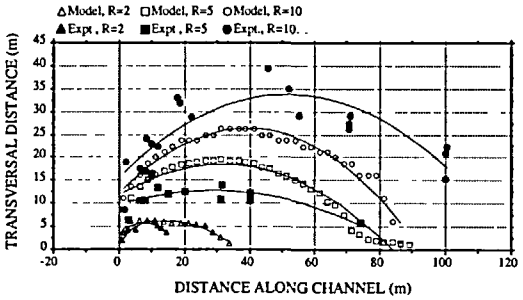

Figure 4 Jet trajectories of warm water discharges

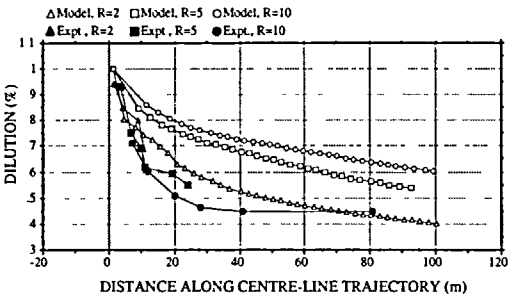

Figure 5 Dilution along centre-line trajectory

Hydrodynamic computations were performed for different side-discharge to channel flow velocity ratio. Jet trajectories of the warm water discharge, dilution of the warm water along the jet trajectory, and reattachment lengths were evaluated for all test cases.

The computed jet trajectory penetration of warm water discharges are compared with predictions obtained by McGuirk and Rodi[11], and with measurements by Carter[5] for three velocity ratios 2, 5 and 10 (*Table 1* and *Figure 4*). The model calculations are slightly overpredicted for velocity ratios 2 and 5 and underpredicted for velocity ratio 10; however, in acceptable agreement with measurements. Also, the present model gives a reasonable improvement to the other numerical model. The deviation in the results for velocity ratio 10 may be due to the proximity of the far bank which affects the penetration of the side discharge. This effect results in the reduction of the side discharge penetration.

The computed dilution of warm water along the jet trajectory is also compared with predictions obtained by McGuirk and Rodi[11], and with measurements by Carter[5], for the three velocity ratios 2, 5 and 10 (*Table 2* and *Figure 5*). Dilution of warm water can be defined as the ratio

Table 3 Evaluation of reattachment lengths

Velocity ratio	Mikhail[13]	McGuirk *et al.*[11]	Model
2	4.9	2.8	3.5
5	5.3	3.2	4.2
10	7.3	3.8	5.0

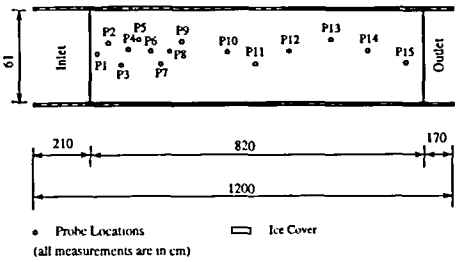

Figure 6 Channel and ice cover initial setup

of the maximum temperature excess over the river temperature and discharge temperature excess over the river temperature. The model calculations show that for velocity ratio 2, the dilution is accurately predicted. With an increase in the velocity ratio, the model tends to overpredict dilution, however with acceptable differences. The dilution predicted by the present model behaves similar to what is deduced from measurements, such that dilution increases with increasing velocity ratio.

Computed reattachment lengths are compared with predictions obtained by McGuirk and Rodi[11], and with measurements by Mikhail *et al.*[13], for the three velocity ratios 2, 5 and 10 (*Table 3*). Both the model computations and those of McGuirk and Rodi[11], underestimate the eddy length, however with the present calculation showing better agreement with experimental data.

Ice cover melting

Data obtained from laboratory measurements, where an ice cover was grown in a flume located in a temperature controlled room, were used for the numerical simulations. After growing the ice cover to the desired thickness, the water temperature was then set to 1°C, thereby allowing the ice to melt. Ice cover thickness was measured at various locations as a function of time.

The channel setup is shown in *Figure 6*. A flume 12 m long and 0.6 m wide was used for the investigations. The initial ice cover was not uniform with an average thickness of 5 cm and a length of 820 cm. Depending on the flow condition, three zones are distinguished: an inlet zone extending 210 cm of open water, followed by an ice covered middle zone of 820 cm, and an outlet zone of 170 cm at the end of the flume. The inlet temperature was maintained at a mean value of 1°C while air temperature was maintained at 0°C. The average discharge per unit width was kept at an approximately constant value of 0.0372 $m^2 s^{-1}$.

Two test runs were performed for the simulation of ice cover melting under turbulent flow conditions. At first, the setup was accurately reproduced in the numerical model. The geometry of the channel was fitted by a uniform grid system with cell sizes of 0.2 m in the longitudinal direction and 0.03 m in the transversal direction. The velocity field was set to a constant value of 0.186 m sec^{-1} and the temperature field to 1°C. The model was run using only the hydrodynamic and thermal energy routines until a steady state is reached. A check for continuity was constantly performed between the entrance and exit of the channel. The air temperature was taken at 0°C. Cloud cover was set to 90% and the barometric pressure to 0.7547 m of Hg. Once steady-state is achieved, ice cover thicknesses were introduced in the model with the exact values as measured in the laboratory at the various probes (*Figure 6*).

The melting pattern characterized by the temporal variation of longitudinal ice cover thickness profiles is presented in *Figure 7* for test run 1 and in *Figure 8* for test run 2. Comparisons between the computed and measured ice cover thickness profiles are shown at 100 minute intervals. The measured and computed melting values compare well throughout the simulation time. However, as apparent from *Figure 7*, the measured melting values in the leading edge

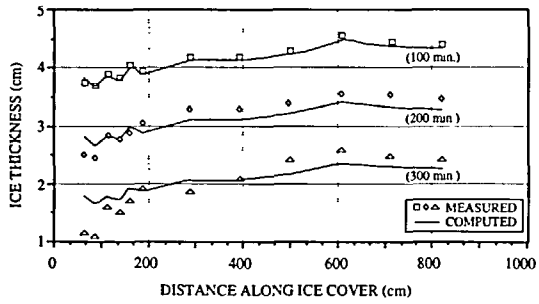

Figure 7 Longitudinal ice cover thickness profile, test case 1

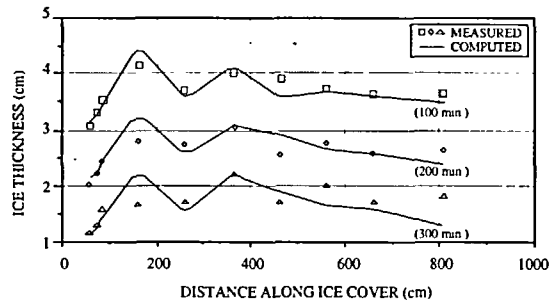

Figure 8 Longitudinal ice cover thickness profile, test case 2

region, for test run 1, shows a noticeable increase in rate and pattern which is not reflected in the computational results.

Looking back at both *Figures 7* and *8*, the relation between measured and computed ice cover thicknesses let identify two distinct melting regions. The first region stretches over a small distance downstream from the leading edge, while the second region extends over the rest of the downstream length of the ice cover. In the leading edge region, simulated ice cover thickness profiles from test run 1 indicate that the predicted profile after 100 minutes of simulation time compares favorably with the measured profile having a percentage difference less than 1%. However, beyond that time, the difference between predicted and measured ice cover thicknesses increase, as shown in *Figure 7* for the 200 and 300 minute profiles, with the predicted ice cover thicknesses smaller than the measured thicknesses. For test run 1, the model under predicted the melting of the ice cover at the leading edge on an average of 5% and 15% at 200 min and 300 min respectively, while slightly over predicted the melting in the downstream region on an average of 3% and 2% at 200 min and 300 min, respectively.

For test run 2, the measured and computed longitudinal ice cover thickness profiles compare well in the leading edge as well as in the downstream region over the simulation period. Unlike test run 1, computed and measured ice thicknesses do not diverge in time but rather their difference remain unchanged by less than 1%. However, at the trailing edge, the difference between measured and computed ice thicknesses shows slight increase. The ice thickness measurement at last probe does not reflect the performance of the numerical model but rather represents an indication of the local ice cover melting conditions for this specific test run. However, when the probe immediately upstream of the last one is considered, then the accuracy of the computed ice cover thicknesses becomes evident.

In spite of the different results between test runs 1 and 2, the fact remains that the numerical formulation and conditions are kept unchanged in the model while during the experimental runs, attempts were made to keep the flow conditions constant. It is evident from the data that the conditions in the experimental test runs were not consistent.

In the leading edge entry region, the water flow has complex and turbulent behaviour, hence the associated thermal conditions are difficult to simulate as by the oscillatory behaviour shown from the experimental data. Also, a larger area of the ice cover is subjected to the flow at the leading edge region. This area in turn varies with time as it melts and assumes a profile that follows the flow streamlines. Turbulence in the entry region also varies with the local ice cover bottom profile which is smoothed as is itself affects the turbulence. As a result to this dynamic phenomenon occurring in the leading edge region, the rate of the ice cover melting assumes a non-linear variation in time. However, in the downstream region the variation in ice cover melting is shown to be linear.

The overall measured and computed melting behaviour of the ice cover is better shown by considering the corresponding average ice cover thickness as it varies in time. The total melting

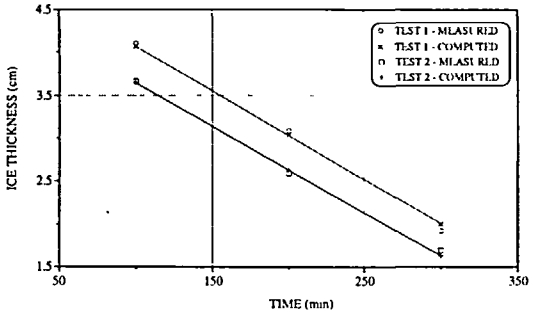

Figure 9 Computed and measured average ice cover thickness, test cases 1 and 2

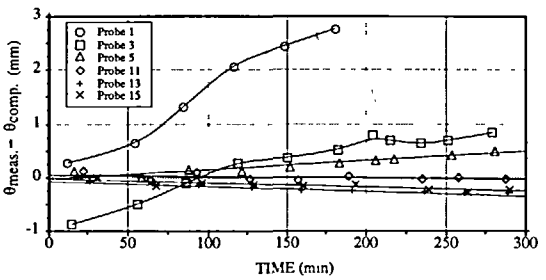

Figure 10 Difference between measured and computed ice thicknesses, test case 1

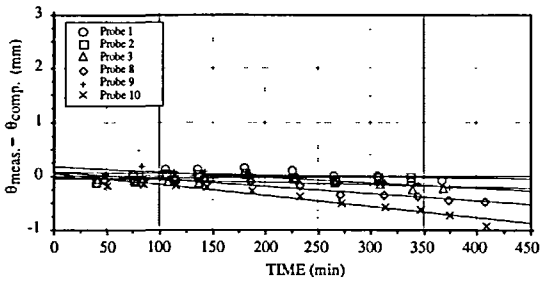

Figure 11 Difference between measured and computed ice thicknesses, test case 2

caused by the flow has been evaluated for test runs 1 and 2. The measured and computed ice cover total melting as a function of time is presented in *Figure 9*, for both tests runs 1 and 2. The average thickness of the ice cover is shown to assume a linear character, and computed results show a good agreement with the measured average ice cover melting.

These findings were confirmed by detailed analysis of the ice cover thickness variation at various locations on the ice cover. The differences between measured and predicted ice cover thicknesses, as a function of time, as shown for six locations in *Figure 10* and *11* for test runs 1 and 2, respectively. The data in these Figures were fitted with curves to help evaluate the variation in the rate of change of the ice thicknesses along the ice cover. The slope of the lines indicates the rate of change between the measured and computed ice melting. Lines with a steep slope indicate larger error rate. A positive slope is an indication of divergence between measured and computed ice cover thicknesses (i.e. the difference is increasing in time), while a negative slope represents convergence between measured and computed ice cover thicknesses (i.e. the difference is decreasing in time). The lines at the leading edge region are characterized by steep positive slopes and non-linear variation in the difference between measured and computed ice cover melting. However, along the downstream region, the slope of the lines decreases and the difference between measured and computed ice cover melting approaches a rather linear behaviour. Similar behaviour is shown for test run 2 with the exception that computed ice cover melting was always underestimated (*Figure 11*). Also, the lines are nearly horizontal indicating smaller difference between measured and computed ice cover melting.

CONCLUSIONS

The melting of an ice cover under turbulent flow conditions was investigated through numerically reproducing two experimental tests. The present work focuses mainly on modelling the influence of warm water on the transient changes in the ice cover thickness under turbulent flow conditions.

The numerical model used in this study helped identify two distinct regions in an ice cover undergoing melting. These regions are the leading edge and trailing edge. A maximum difference between measured and computed ice cover thickness of less than 4% in the downstream region and 12% in the leading edge region was obtained for test run 1. However, this difference between measured and computed thicknesses was evaluated at less than 1% in the leading edge region and approximately 7% in the trailing edge region.

The total amount of melting of the ice cover is predicted within 5% for test runs 1 and 2. In both test runs, the melting pattern in the leading edge region was found to behave differently from that in the trailing edge region of the ice cover. The melting of an ice cover in the downstream region can be simulated with good accuracy using the presented set of formulations is needed to account for the non-linear melting behaviour in this region.

ACKNOWLEDGEMENTS

This work was supported by NSERC-A-4899 grants which are gratefully acknowledged.

REFERENCES

1 Anderson, E. R. Energy budget studies, in *Water-Loss Investigations: Lake Hefner Studies, TR, US Geol. Survey, Prof. Paper 269*, pp. 71–118 (1954)
2 Ashton, G. D. Suppression of river ice by thermal effluents, *CRREL Report 79-30*, US Army Cold Regions Research Engineering Laboratory, Hanover, NH (1979)
3 Baldwin, B. S., MacCormack, R. W. and Diewart, G. S. Numerical techniques for the solution of the compressible Navier–Stokes equations and implementation of turbulence models, *AGARD Lecture Series No. 73*, NATO, London, pp. 2.1–2.22 (1975)
4 Bilello, A. M. Water temperatures in a shallow lake during ice formation, growth and decay, *Water Resources-Res.*, **4** (1968)
5 Carter, H. H. A preliminary report on the characteristics of a heated jet discharged horizontally into a transverse current. Part I—Constant depth, Chesapeake Bay Inst., *Johns Hopkins Univ. Tech. Rep. no. 61* (1969)
6 Chapman, S. R. A numerical simulation of two-dimensional separated flow in a symmetric open-channel expansion using the depth integrated two-equation (*k*-epsilon) turbulence closure model, *PhD Thesis*, Virginia Polytechnic Institute and State University (1982)
7 Colburn, A. P. A method of correlating forced convection heat transfer data and comparison with liquid frictions, *Trans. AICHE*, **29**, 174–210 (1933)
8 Dingman, S. L., Weeks, W. F. and Yen, Y. C. The effects of thermal pollution on river ice conditions, Part 1, A general method of calculation, *CRREL Report 206*, US Army Cold Regions Research Engineering Laboratory, Hanover, NH (1967)
9 Hewlett, Y. B. Rate of recession of the leading edge of ice covers on open channel flows, *Masters Thesis*, University of Iowa (1976)
10 Marsh, P. and Prowse, T. D. Water temperature and heat flux at the base of river ice covers, *Cold Regions Sci. Technol.*, **14**, 33–50 (1987)
11 McGuirk, J. J. and Rodi, W. A depth-averaged mathematical model for the near field of side discharges into open-channel flow, *J. Fluid Mech.*, **86**, 761–781 (1978)
12 Michel, B. Winter regime of rivers and lakes, *Monogr. III-B1a*, US Army Corps of Engineers, Cold Regions Research and Engineering Laboratory (1971)
13 Mikhail, R., Chu, V. H. and Savage, S. B. The reattachment of a two-dimensional turbulent jet in a confined cross flow, *Proc. 16th IAHR Cong., Sao Paulo*, 3, 414–419 (1975)
14 Paily, P. P., Macagno, E. O. and Kennedy, J. F. Winter-regime surface heat loss from heated streams, *IIHR Report No. 155*, Iowa Institute of Hydraulic Research (1974)
15 Patankar, S. V. *Numerical Heat Transfer and Fluid Flow*, Hemisphere, Washington, DC (1980)

16 Raithby, G. D. A critical evaluation of upstream differencing applied to problems involving fluid flow, *Comp. Meth. Appl. Mech. Eng.*, **9**, 75–103 (1976)
17 Rodi, W. *Turbulence models and their application in hydraulics—a state of the art review*, University of Karlsruhe (1980)
18 Saadé, R. Numerical modelling of ice cover melting under turbulent flow conditions, *MASc Thesis*, Concordia University (1990)
19 Sarraf, S. and Saleh, W. Local melting of ice cover by thermal side effluent, *Cold Regions*, **1**, 105–122 (1987)
20 Sarraf, S. Heated effluent effects on ice covered rivers, *ASCE Cold Regions Eng.*, **4**, 161–178 (1990)
21 Shen, T. S. and Chiang, L. Simulation of growth and decay of river ice cover, *J. Hyd. Eng. ASCE*, **110**, 958–971 (1984)
22 Shen, H. T., Bjedov, G., Daly, S. F. and Wasantha, A. M. Numerical model for forecasting ice conditions on the Ohio river, *CRREL Report 91-16* (1991)